Evaluation of Parameterizations of Incoming Longwave Radiation in the High-Mountain Region of the Tibetan Plateau

MEILIN ZHU

Key Laboratory of Tibetan Environment Changes and Land Surface Processes, Institute of Tibetan Plateau Research, Chinese Academy of Sciences, Beijing, China

TANDONG YAO, WEI YANG, AND BAIQING XU

Key Laboratory of Tibetan Environment Changes and Land Surface Processes, Institute of Tibetan Plateau Research, Chinese Academy of Sciences, and Chinese Academy of Sciences Center for Excellence in Tibetan Plateau Earth Sciences, Beijing, China

XIAOJUN WANG

Institute of Agricultural Economics and Development, Chinese Academy of Agricultural Sciences, Beijing, China

(Manuscript received 21 May 2016, in final form 25 November 2016)

ABSTRACT

Accurate evaluations of incoming longwave radiation (L_{in}) parameterization have practical implications for glacier and river runoff changes in high-mountain regions of the Tibetan Plateau (TP). To identify potential means of accurately predicting spatiotemporal variations in L_{in}, 13 clear-sky parameterizations combined with 10 cloud corrections for all-sky atmospheric emissivity were evaluated at five sites in high-mountain regions of the TP through temporal and spatial parameter transfer tests. Most locally calibrated parameterizations for clear-sky and all-sky conditions performed well when applied to the calibration site. The best parameterization at five sites is Dilley and O'Brien's A model combined with Sicart et al.'s A for cloud-correction-incorporated relative humidity. The performance of parameter transferability in time is better than that in space for the same all-sky parameterizations. The performance of parameter transferability in space presents spatial discrepancies. In addition, all all-sky parameterizations show a decrease in performance with increasing altitude regardless of whether the parameters of all-sky parameterizations were recalibrated by local conditions or transferred from other study sites. This may be attributable to the difference between screen-level air temperature and the effective atmospheric boundary layer temperature and to different cloud-base heights. Nevertheless, such worse performance at higher altitudes is likely to change because of terrain, underlying surfaces, and wind systems, among other factors. The study also describes possible spatial characteristics of L_{in} and its driving factors by reviewing the few studies about L_{in} for the mountain regions of the TP.

1. Introduction

Incoming longwave radiation L_{in} is a critical component of the energy budget of Earth's surface. It plays a major role in climate change, glacier change, and river runoff change in high-mountain regions of the Tibetan Plateau (TP). First, increased L_{in} levels resulting from increasing specific humidity and cloud cover spur surface warming on the TP (Philipona et al. 2005; Rangwala and Miller 2012). Second, L_{in} constitutes the most significant source of energy for glacier melt in many environments (Ohmura 2001; Sedlar and Hock 2009). This is key to understanding the physical mechanisms of spatially heterogeneous changes on Tibetan glaciers (Yao et al. 2012; Gardelle et al. 2012). Third, precise L_{in} measurements are conducive to yielding accurate simulation results of evapotranspiration and glacier discharge, which is essential for glacier hazard prevention, oasis agricultural water downstream, and even the socioeconomic development of the TP as a whole. Above all, it is very important to obtain accurate L_{in} values for the TP.

The observed L_{in} data are very poor because of high instrument measurement costs and difficulties associated

Corresponding author e-mail: Meilin Zhu, meilinzhu@itpcas.ac.cn

DOI: 10.1175/JAMC-D-16-0189.1

with traveling to high-altitude regions. A lack of observed L_{in} data further complicates glacier and runoff change quantifications on the TP under conditions of global warming. The L_{in} data can be obtained from satellites (W. Wang and Liang 2009). However, such data are much less accurate than data predicted using the surface database model over regions of highly varying elevations, especially for the Himalayas (K. Yang et al. 2010). The L_{in} values can also be obtained through numerical simulations based on models. These models can be classified into three main categories: 1) radiative transfer models, 2) models with some specifications on the vertical structure of the atmosphere, and 3) simple parameterizations (Dilley and O'Brien 1998). The first two models are difficult to use because it is not easy to obtain the data that are required to satisfy the model. Simple parameterizations can calculate L_{in} by using screen-level meteorological variables alone without more detailed data. All of the models tested in this work belong to the simple parameterizations, which have been applied effectively in energy balance models for mountain glaciers (Klok and Oerlemans 2002; Mölg et al. 2009; Yang et al. 2013).

Previous studies have evaluated the performance of parameterizations of L_{in} around the world (e.g., Prata 1996; Niemelä et al. 2001; Iziomon et al. 2003; Flerchinger et al. 2009; Abramowitz et al. 2012; Marthews et al. 2012; Carmona et al. 2014). Nevertheless, the performances of these parameterizations have varied, with varying parameters found even for the same parameterization applied to different climatic regions (Alados et al. 2012; Gubler et al. 2012; MacDonell et al. 2013). No single parameterization has been selected as the most appropriate means of modeling L_{in} in different regions. The parameters adopted from the literature will likely generate considerable errors in simulating L_{in} for other places (MacDonell et al. 2013), further resulting in significant underestimations of glacier melt (Juszak and Pellicciotti 2013). Therefore, parameter calibration is necessary for parameterization, and the best parameterization must be recognized to estimate accurate L_{in} values in space and time (K. Wang and Liang 2009; Yang et al. 2013).

Recent studies have strictly focused on optimizing the parameters of a single parameterization for a fixed location on the TP (e.g., K. Yang et al. 2010; Yang et al. 2011; Zhu et al. 2015). Detailed comparisons of the performance of different parameterizations have not been carried out for the mountainous environment on the TP. In this work, data from five high-altitude automatic weather stations (AWSs) on or near the glacier on the TP under different climatic conditions offer opportunities 1) to compare the performance of parameterizations of L_{in} proposed in the literature for clear-sky and all-sky conditions in the mountain environment, 2) to investigate the transferability of parameterizations in time and space, and 3) to examine the spatial pattern of L_{in} by reviewing recently published L_{in} data for the TP. These results will prove useful for studying glacier mass balance and meltwater discharge on a regional scale for the last decade on the TP.

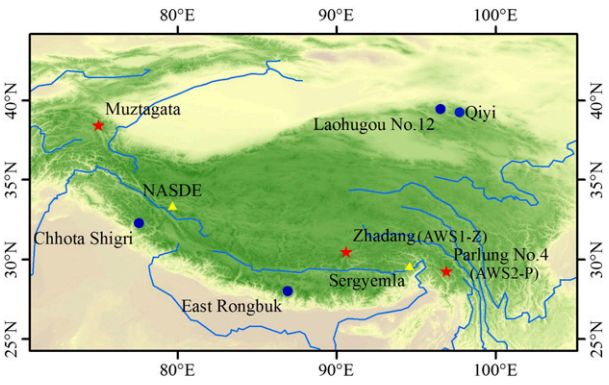

FIG. 1. Map showing the location of the Muztagata region, Zhadang Glacier, and Parlung 4 Glacier (red stars) on the TP, two selected sites (NASDE and the Sergyemla Mountains) with daily meteorological measurements (yellow triangles) used to test the performance of the best all-sky parameterization, and four sites with published L_{in} data (blue circles) used to analyze the spatial distribution of L_{in}.

2. Research area and data

a. Study region

Figure 1 shows the locations of the three study regions on the TP. Muztagata is situated in eastern Pamir at the northwestern end of the TP (Fig. 1), where the climate is controlled by westerlies all year and is not influenced by the South Asian monsoon (Tian et al. 2007). The annual mean precipitation is roughly 75 mm, and the main precipitation period occurs from April to September according to data records from the Tashkurghān meteorological station (37°47′N, 75°14′E, 3100 m). Zhadang and Parlung 4 Glaciers are located in the southern central and southeastern areas of the TP, respectively (Fig. 1), where climatic patterns are affected by the South Asian monsoon in the summer and by westerlies in the winter. The annual mean precipitation is 479 mm at the Damxung meteorological station (30°29′N, 91°06′E, 4200 m, roughly 44 km from Zhadang Glacier) and 792 mm at the Zayu meteorological station (28°39′N, 97°28′E, 2327.6 m, roughly 90 km from Parlung 4 Glacier). Precipitation at Zhadang Glacier concentrates in the summer and occurs mainly from the spring to the summer at Parlung 4 Glacier (Zhu et al. 2015).

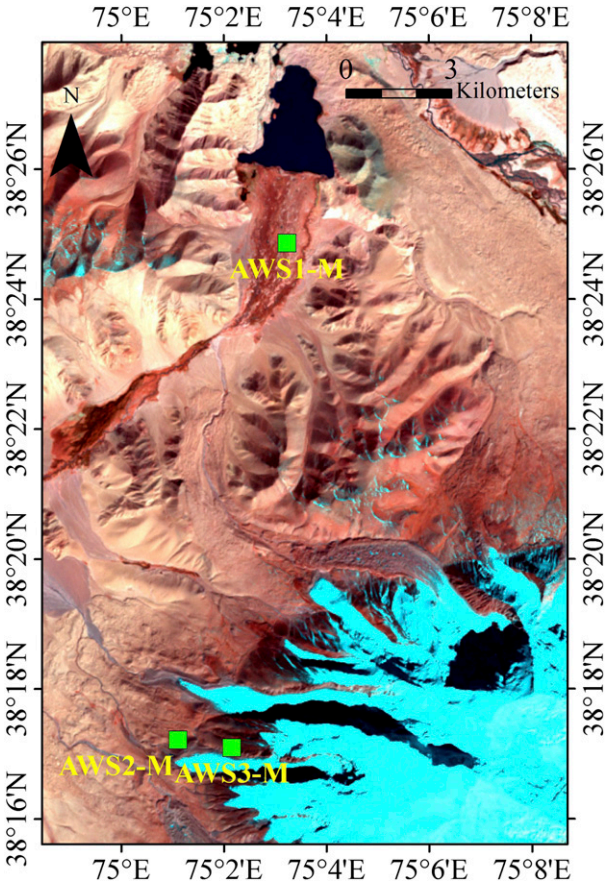

FIG. 2. Location of the three AMSs in the Muztagata region. The background satellite image is taken from Landsat ETM+ (2006).

b. Data

Three AWSs (AWS1-M, AWS2-M, and AWS3-M) are installed in the Muztagata region. Their locations are shown in Fig. 2. AWS1-M, which is located on sandy ground, was installed in October 2009. AWS2-M was installed at the foot of a mountain slope in July 2011, and AWS3-M was installed on a hillside close to the glacier in August 2011. AWS1-M and AWS2-M (AWS2-M and AWS3-M) are positioned approximately 14.3 km (1.5 km) apart. The meteorological variables stored in Campbell Scientific, Inc., CR1000 dataloggers of the three AWSs include air temperature (T), relative humidity (RH), vapor pressure (e), wind speed (WS), wind direction (WD), incoming shortwave radiation (S_{in}), reflected shortwave radiation (S_{out}), L_{in}, and outgoing longwave radiation (L_{out}). These variables are treated as hourly averages that drive parameterization of L_{in}. Characteristics and basic information for these sensors are listed in Table 1.

AWS1-P sensors at 4800 m MSL on Parlung 4 Glacier are similar to AWS1-M sensors in the Muztagata region, but AWS1-Z sensors at 5665 m MSL on Zhadang Glacier are different from other AWSs (Table 1). The L_{in} was not directly measured at AWS1-Z but is calculated as a residual based on measured net radiation, glacier surface temperature, S_{in}, and S_{out}. For detailed information on the two AWSs, please refer to Yang et al. (2011) and Zhu et al. (2015).

To ensure high data quality, the measured L_{in} needed to be calibrated. First, L_{in} data were separated into several groups binned at 1-K intervals of T. The L_{in} data for each group were deleted when values fell outside the ± 2 standard deviation (STD) range. Second, a lack of ventilation for the AWS pyranometers or the wintertime riming could cause deviations in the measured L_{in} (Van den Broeke et al. 2004). These data with the above deviations were discerned from the method presented by Van den Broeke et al. (2004) and were removed for modeling L_{in} better.

Basic T, RH, e, WS, effective cloud cover fraction (n_{eff}), L_{in}, and S_{in} statistics are listed in Table 2, which shows the differences in mean behavior and variability among the meteorological records at five AWSs. This means that the climate regime is different in three study regions. Relative to the Muztagata region under the influence of westerlies, two other study regions that are affected by the South Asian monsoon show higher T, RH, e, n_{eff}, and L_{in} values and lower WS and S_{in} values. The measurement periods of each AWS are also listed in Table 2.

3. Methods

The L_{in} is modeled using the Stefan–Boltzmann equation for a graybody:

$$L_{\text{in}} = \varepsilon_a(T,e)\sigma T^4 = \varepsilon_{\text{cs}}(T,e)F\sigma T^4, \qquad (1)$$

where ε_a is the all-sky effective emissivity, T is the screen air temperature (K), e is vapor pressure (Pa), σ is the Stefan–Boltzmann constant ($5.67 \times 10^{-8}\,\text{W m}^{-2}\,\text{K}^{-4}$), and ε_{cs} is the effective emissivity of the clear-sky condition, which is estimated using different empirical parameterizations. The term F is the cloud emission factor, which is calculated through cloud corrections based on the cloud cover estimation; $F = 1$ is identified as a clear-sky condition with no clouds in the sky; $F > 1$ indicates that L_{in} will be influenced by cloud cover. Two key issues need to be addressed in this study: 1) ways to quantify clear-sky periods and cloud cover and 2) ways to evaluate the performance of different parameterizations.

a. Clear-sky conditions and cloud cover

The clear-sky parameterizations are only fit for periods without clouds, and thus, we must discern clear-sky

TABLE 1. Sensor information at AWSs with their technical specifications.

Parameter	Sensor	Accuracy	Location
T	Vaisala, Inc., HMP 45C	±0.2°C (from −40° to +60°C)	AWS1-M, AWS2-M, AWS3-M, AWS2-P
	Campbell CS215	±0.9°C (from −40° to +70°C)	AWS1-Z
RH	Vaisala HMP 45C	±2% (0%–100%)	AWS1-M, AWS2-M, AWS3-M, AWS2-P
	Campbell CS215	±4% (0%–100%)	AWS1-Z
WS	R. M. Young Co. 05103 wind monitor	±0.3 m s^{-1}	AWS1-M, AWS2-M, AWS3-M, AWS2-P, AWS1-Z
S_{in}	Kipp and Zonen B.V. CNR1	±10%	AWS1-M, AWS2-M, AWS3-M, AWS2-P
	Campbell CS300	5% for daily totals	AWS1-Z
L_{in}	Kipp and Zonen CNR1	±10%	AWS1-M, AWS2-M, AWS3-M, AWS2-P
	A residual from measured incoming/outgoing shortwave and net radiation and surface temperature		AWS1-Z

conditions from cloudy conditions. The clear-sky index (CSI) proposed by Marty and Philipona (2000) can separate clear-sky conditions from cloudy-sky conditions based on measurements of L_{in}, e, and T. CSI ≤ 1 is identified as the clear-sky condition, and the remaining data are classified as cloudy-sky conditions.

Cloud cover, as an input variable in the cloud correction formula, is difficult to measure and cannot be well observed. Therefore, various parameterizations have been developed to estimate the cloud cover (e.g., Crawford and Duchon 1999; Sicart et al. 2006). Commonly used parameterizations include n_{eff} or bulk atmospheric transmissivity (τ_{atm}), which are based on the measured S_{in} (MacDonell et al. 2013). The two parameterizations are easy to calculate and have shown good performance in modeling L_{in} (Sicart et al. 2006; Gubler et al. 2012). Therefore, we use the two cloud parameterizations in this study.

The hourly n_{eff} is calculated as the ratio of the measured S_{in} and the clear-sky solar radiation (S_{clear}) (e.g., Crawford and Duchon 1999; K. Yang et al. 2010). The S_{clear} is computed using a nonparametric model described by K. Yang et al. (2010). We can determine the n_{eff} as follows:

$$n_{eff} = 1 - S_{in}/S_{clear}. \quad (2)$$

In addition, the τ_{atm} can be used to infer a cloud cover index (Sedlar and Hock 2009; Sicart et al. 2010). Its computational formula is as follows:

$$\tau_{atm} = 1 - S_{in}/S_{TOA}, \quad (3)$$

where S_{TOA} is the amount of clear-sky shortwave radiation at the top of the atmosphere.

The two cloud parameterizations are based on the measured S_{in}, and thus, no cloud information can be obtained at night. Nighttime is defined as $S_{clear} < 200\,W\,m^{-2}$. To solve this problem, the liner interpolation of the mean n_{eff} and τ_{atm} between the last three hours of the day prior and the first three morning hours of the following day are used to obtain nighttime cloud information (Juszak and Pellicciotti 2013). Relative to other methods that address nocturnal cloud cover, this approach slightly improves the simulation accuracy of all-sky parameterizations. The correlation coefficients between longwave-equivalent cloudiness proposed by Van den Broeke et al. (2006) and Kuipers Munneke et al. (2011) and n_{eff} and between longwave-equivalent cloudiness and τ_{atm} are 0.58 and −0.59 ($p < 0.05$), respectively. The cloud cover models proposed by other authors (Kasten and Czeplak 1980; Konzelmann et al. 1994; Greuell et al. 1997; Sedlar and Hock 2009) are also tested, and the correlation coefficients of the estimated cloud cover with measured L_{in} are similar to n_{eff} and τ_{atm}. Therefore, n_{eff} and τ_{atm} can be used as good indexes for cloud cover.

b. Calibration and validation

The performance of parameterizations can be evaluated based on the root-mean-square error (RMSE), the mean bias error (MBE), and a comparison between the observed and predicted STD. A negative (positive) MBE value denotes an underestimate (overestimate) of L_{in} in the parameterization. These indicators have been effectively used to assess the accuracy of the model (Gubler et al. 2012; Sedlar and Hock 2009). However, although the values of RMSE may vary slightly, the MBEs vary considerably among different parameterizations of L_{in} (MacDonell et al. 2013). Therefore, the sum of RMSE and |MBE| (RMSEb) is taken as the main index used to assess the performance of parameterizations.

4. Results

a. Parameter calibration for clear-sky parameterizations

We calibrated 13 clear-sky parameterizations (Table 3) based on clear-sky daytime condition (CSI ≤ 1) for 2010 at AWS1-M using the least squares fitting method

TABLE 2. Characteristics of the locations of the AWSs on each site; the mean values (STD) of meteorological factors; and the correlation coefficient ($p < 0.001$ unless stated) of measured L_{in} with T, RH, e, and n_{eff} at each AWS for 2012.

		AWS1-M	AWS2-M	AWS3-M	AWS2-P	AWS1-Z
Geography	Location	Muztagata	Muztagata	Muztagata	Parlung 4	Zhadang
	Lat (°N)	38°24′52″	38°17′13″	38°17′6″	29°15′7″	30°28′17″
	Lon (°E)	75°3′14″	75°1′6″	75°2′9″	96°55′53″	90°38′43″
	Alt (m MSL)	3655	4400	4900	4800	5665
	Sky view factor	0.99	0.94	0.84	0.91	0.97
	Environment	Grass	Rock	Rock	Glacier	Glacier
	Measurement period	23 Oct 2009–29 Oct 2013	17 Jul 2011–10 Oct 2013	21 Aug 2011–11 Jul 2013	21 May–9 Sep 2009 11 Sep 2010–27 Mar 2011 5 Jan 2012–26 Sep 2013	27 Apr–15 Jul 2009 30 Sep 2009–26 Jun 2010 15 Aug 2010–21 Sep 2013
Average (STD)	T (°C)	−0.79 (9.4)	−5.3 (9.4)	−8.9 (8.2)	−3.6 (6.9)	−7.1 (8.8)
	RH (%)	49 (23)	49 (24)	54 (24)	69 (19)	57 (23)
	e (kPa)	0.33 (0.23)	0.24 (0.19)	0.2 (0.16)	0.37 (0.22)	0.25 (0.2)
	WS ($m\,s^{-1}$)	3.4	3.5	3.6	2.4	2.3
	n_{eff}	0.27 (0.2)	0.32 (0.23)	0.32 (0.24)	0.4 (0.26)	0.33 (0.2)
	L_{in} ($W\,m^{-2}$)	249 (52)	224 (53)	210 (54)	245 (62)	219 (38)
	S_{in} ($W\,m^{-2}$)	209 (295)	211 (304)	215 (315)	203 (310)	205 (307)
Correlation	L_{in} and T	0.82	0.75	0.69	0.76	0.8
	L_{in} and RH	0.28	0.6	0.62	0.7	0.4
	L_{in} and e	0.83	0.83	0.84	0.88	0.74
	L_{in} and n_{eff}	0.29	0.05	0.1	0.6	0.24

(Lhomme et al. 2007; MacDonell et al. 2013). The daytime condition that is defined as $S_{clear} \geq 200\,W\,m^{-2}$ is used to distinguish between day and night in this study, thereby reducing the n_{eff} value uncertainty. The n_{eff} is largely affected by the terrain when sun angles are low ($S_{clear} < 200\,W\,m^{-2}$).

Table 3 shows the original and locally calibrated parameters for the clear-sky parameterizations. The calibrated parameters are different from their original values. The differences between calibrated and original values for some parameters are small but for others are large even for the same parameterization. This is in line with the analyses by MacDonell et al. (2013) and Carmona et al. (2014) that show that these parameters vary in different locations.

In addition, almost all of the clear-sky parameterizations with original values perform worse than those based on locally calibrated parameters (Table 3). The RMSE values of the models with original coefficients range from 13 to ~73 $W\,m^{-2}$, which are obviously higher values than those of models with locally calibrated parameters (Table 3). Therefore, we use equations with locally calibrated coefficients to estimate L_{in} under clear-sky conditions at AWS1-M.

When using locally calibrated parameters, most of the 13 clear-sky parameterizations yield similarly good RMSE values of within 11 $W\,m^{-2}$ in 2010, with the exception of Swinbank's (1963), Idso and Jackson's (1969), and Maykut and Church's (1973) models (Table 3). The above three worst clear-sky parameterizations will not be combined with the cloud correction formula in the next phase. The best results are derived from Brutsaert's (1975), Dilley and O'Brien's (1998) A and B, and Konzelmann et al.'s (1994) models (Table 3). The MBE for clear-sky parameterizations is close to zero. The modeled STD is comparable to the measured STD (44.7 $W\,m^{-2}$) for clear-sky conditions. In addition, most clear-sky parameterizations with e as an input are better than equations with only T as an input, in agreement with Carmona et al. (2014).

b. *Parameter estimation of all-sky parameterizations*

Table 4 shows common parameterizations of emissivity for cloudy conditions. Crawford and Duchon's (1999) parameterization is similar to Konzemann et al.'s (1994) formula. Thus, we only analyze Konzelmann et al.'s (1994) formula in the study. The 10 cloud corrections combined with each of the calibrated clear-sky parameterizations are used to model L_{in} (Juszak and Pellicciotti 2013). All hourly data in 2010 from AWS1-M are used to calibrate these all-sky parameterizations. An important factor when calculating all-sky parameterizations is cloud cover, which is considered in some all-sky parameterizations. Meanwhile, some all-sky parameterizations do not consider cloud cover, where L_{in} is calculated directly using T and humidity (Table 5). The MBEs of four all-sky parameterizations without cloud correction at AWS1-M are 0.37, −0.51, 1.54, and 0.03 $W\,m^{-2}$ (Table 5). The RMSEs are 27, 24.1, 36, and

TABLE 3. Parameterizations of clear-sky emissivity (ε_{cs}), RMSE (W m^{-2}), and MBE (W m^{-2}) of estimated L_{in} of clear-sky conditions for the AWS1-M site in daytime. The quantity w is the precipitable water (kg m^{-2}), which is estimated using the approach suggested by Prata (1996); h (m) is the elevation of the AWS (m); e (Pa) is vapor pressure at screen level for most parameterizations except for Brutsaert's (1975) formula (hPa); T (K) is air temperature at screen level.

Source	Code	Parameterization	Optimized (original) parameter	RMSE Optimized (original)	MBE Optimized (original)
Brunt (1932)	CBR	$\varepsilon_{cs} = a + b\sqrt{e}$	a = 0.6 (0.47), b = 0.0076 (0.0072)	9.5 (48)	0.1 (−46)
Brutsaert (1975)	CBT	$\varepsilon_{cs} = a(e/T)^b$	a = 1.12 (1.24), b = 10.8 (7)	9.5 (33)	0.1 (−31)
Dilley and O'Brien (1998), A	CDOA	$\varepsilon_{cs} = 1 - \exp\{-1.66[(aT/173.16) + c\sqrt{w/25}]\}$	a = 0.164 (2.232), b = 0.3323 (−1.875) c = 0.6715 (0.7356)	9.5 (31)	0 (−26)
Dilley and O'Brien (1998), B	CDOB	$\varepsilon_{cs} = [a + b(T/173.16)^6 + c\sqrt{w/25}]/\sigma T$	a = 30 (59), b = 157 (113), c = 97.73 (96.96)	9.5 (24)	0 (−20)
Garratt (1992)	CGA	$\varepsilon_{cs} = a + b\exp(-ce)$	a = 0.83 (0.79), b = 0.21 (0.17), c = 0.0027 (0.000 96)	9.6 (26)	0.1 (−23)
Idso and Jackson (1969)	CIJ	$\varepsilon_{cs} = 1 - a\exp[-b(273 - T)^2]$	a = 0.286 (0.261), b = 0.0007 (0.000 77)	17 (19)	1 (9)
Idso (1981)	CID	$\varepsilon_{cs} = a + be\exp(1500/T)$	a = 0.661 (0.7), $b = 1.03 \times 10^{-6}$ (5.95×10^{-7})	11 (13)	1 (4)
Iziomon et al. (2003)	CIZ	$\varepsilon_{cs} = 1 - a\exp(-be/T)$	$a = 5.17\ (6.26) \times 10^{-5}$ h + 0.1608 (0.336 72), $b = 2\ (1.17) \times 10^{-5}$ h + 0.1656 (0.097 51)	10 (73)	0.3 (−72)
Konzelmann et al. (1994)	CKO	$\varepsilon_{cs} = 0.23 + a(e/T)^b$	a = 0.503 (0.443), b = 7.4 (8)	9.5 (23)	0.1 (−20)
Maykut and Church (1973)	CMC	$\varepsilon_{cs} = a$	a = 0.7344 (0.7855)	18 (25)	1.4 (19)
Niemelä et al. (2001)	CNI	$\varepsilon_{cs} = a + b(e - c)$	a = 0.72 (0.72), c = 193 (200) b = 0.000 16 (0.000 09) for $e \geq 200$ b = 0.000 55 (−0.000 76) for $e < 200$	9.7 (23)	0.1 (8)
Prata (1996)	CPR	$\varepsilon_{cs} = 1 - (1 + w)\exp[-(a + bw)^{0.5}]$	a = 0.91 (1.2), b = 4.18 (3)	9.6 (14)	0.1 (−6)
Swinbank (1963)	CSW	$\varepsilon_{cs} = 10^{a+1}T^{b-4}/\sigma$	a = −12.09 (−13.638), b = 5.516 (6.148)	15 (15)	0 (−2)

27.1 W m^{-2}, respectively. The best parameterization performance without cloud correction provided by Mölg et al.'s (2008) equation is worse than that of most all-sky parameterizations coupled with cloud corrections. Hence, the cloud correction formula can improve the performance of all-sky parameterizations.

For AWS1-M in 2010, the largest RMSE and MBE values are derived from König-Langlo and Augstein's (1994) equation and from Idso's (1981) model combined with Kimball et al.'s (1982) cloud correction (Table 6). The RMSEs and MBEs of the remaining parameterizations are comparable. The largest differences between RMSEs and MBEs for these combinations are less than 0.5 and 0.9 W m^{-2}. Instead, most all-sky parameterizations can estimate L_{in} equally well at one site when the all-sky parameterizations are recalibrated. Thus, relative to the model selection considerations, the calibration of all-sky parameterizations is more important to accurately obtain L_{in} for a single site. This conclusion reflects that of Juszak and Pellicciotti (2013).

c. *Parameter transferability in time*

In sections 4a and 4b, we presented model performance levels with parameters calibrated in 2010 at AWS1-M. Here, we target parameter transferability in time, which can effectively fill data gaps and prolong the time series of L_{in} data. This allows one to produce realistic results for another year by using calibrated all-sky parameterizations for 2010 at AWS1-M.

TABLE 4. Parameterizations of emissivity for cloud conditions. The parameterization of Crawford and Duchon (1999) is similar to the formula of Konzelmann et al. (1994). Thus, we only analyze the formula of Konzelmann et al. (1994) in the study.

Source	Code	Parameterization
Lhomme et al. (2007)	LH	$\varepsilon_a = \varepsilon_{cs}(a + bn)$
Crawford and Duchon (1999)	CD	$\varepsilon_a = \varepsilon_{cs}(1 - n) + n$
Kimball et al. (1982)	KI	$\varepsilon_a = \varepsilon_{cs} + \tau_8 n f_8$ $f_8 = -0.6732 + 6.24 \times 10^{-3} T - 9.14 \times 10^{-6} T^2$ $\tau_8 = 1 - \varepsilon_{8z}(a - b\varepsilon_{8z})$ $\varepsilon_{8z} = 0.24 + 2.98 \times 10^{-6}(e/1000)^2 \exp(3000/T)$
König-Langlo and Augstein (1994)	KA	$\varepsilon_a = a + bn^c$
Konzelmann et al. (1994)	KO	$\varepsilon_a = \varepsilon_{cs}(1 - n^a) + bn^a$
Marshunova (1966)	MA	$\varepsilon_a = (1 + an)(b + c\sqrt{e/100})$
Maykut and Church (1973)	MC	$\varepsilon_a = \varepsilon_{cs}(1 + an^b)$
Mölg et al. (2009)	MG	$\varepsilon_a = \varepsilon_{cs}(a + bn + cn^2 + dn^3)$
Sicart et al. (2006), A	SA	$\varepsilon_a = \varepsilon_{cs}(a + b \times \mathrm{RH} + c\tau_{atm})$
Sicart et al. (2006), B	SB	$\varepsilon_a = \varepsilon_{cs}(a + b\tau_{atm}^c)$
Unsworth and Monteith (1975)	UM	$\varepsilon_a = \varepsilon_{cs}(1 + an) + (bn)$

Table 7 shows the performance of all-sky parameterizations from the temporal parameter transfer tests for the whole observation period without data for 2010. The difference in RMSEbs among different all-sky parameterizations [except for König-Langlo and Augstein's (1994) model] is less than 0.5 W m^{-2}. RMSE and |MBE| values range from 19.9 to 20.4 W m^{-2} and from 0.1 to 0.6 W m^{-2}, respectively. The modeled STDs based on some all-sky parameterizations—for example, Idso's (1981) model combined with Mölg et al.'s (2009) cloud correction, Brutsaert's (1975) model combined with Sicart et al.'s (2006) B cloud correction, and Dilley and O'Brien's (1998) A model combined with Sicart et al.'s (2006) B cloud correction with respective STDs of 46.4, 48.9, and 48.9 W m^{-2}—are comparable to the STD of the observed L_{in} (49.6 W m^{-2}).

To estimate parameter transferability capacities in time, the performance of all-sky parameterizations calibrated for 2010 was compared with that for the other years from temporal parameter transfer tests conducted at AWS1-M (Tables 6 and 7). The mean RMSEb for the observation periods without those for 2010 is 20.6 W m^{-2}, which is only 1 W m^{-2} larger than that for 2010 (Tables 6 and 7). The difference in RMSE between the two periods for all all-sky parameterizations at AWS1-M varied from 0.5 to 1.4 W m^{-2}. The difference in MBE between both periods is less than 0.7 W m^{-2} for each parameterization. In addition, the performance of all-sky parameterizations from temporal parameter transfer tests was compared with that from parameters recalibrated for the other years without those for 2010 at AWS1-M (Table 7). The largest difference in RMSEbs for most all-sky parameterizations is less than 0.5 W m^{-2}. Thus, temporal parameter transfer tests of most all-sky parameterizations produce good modeling results for other years at AWS1-M.

d. *Parameter transferability in space*

In the Tibetan mountain region, measured L_{in} values are only available for a few locations. To obtain L_{in} values of a larger scope where observation data are lacking, a model calibrated for locations must be used to produce realistic results for another location (parameter transferability in space). To assess the validity of parameter transferability in space, parameters of all-sky parameterizations calibrated at AWS1-M are used to model L_{in} for four other sites with their corresponding meteorological data.

At AWS2-M, the mean RMSEb of all parameterizations is 28.6 W m^{-2}, and the performance is slightly poorer than that at AWS1-M (Table 8). The best three parameterizations are Dilley and O'Brien's (1998) A model combined with Sicart et al.'s (2006) A cloud correction, Dilley and O'Brien's (1998) B model combined with Sicart et al.'s (2006) A cloud correction, and Brutsaert's (1975) model combined with Sicart et al.'s (2006) A cloud correction (Table 8). The corresponding RMSEs are 26.3, 26.3, and 26.2 W m^{-2}, respectively. The MBEs are 1.6, 1.8, and 1.9 W m^{-2}, respectively. The STD measurement (49.5 W m^{-2}) can be effectively reflected by the three models with respective STDs of 42.2, 41.7, and 42.3 W m^{-2}. The difference in RMSEbs between the spatial parameter transfer tests and the control tests (recalibrated coefficient for local conditions at AWS2-M) ranges from 2.4 to 3.1 W m^{-2} for the three all-sky parameterizations.

The second validation site is AWS3-M. The best three parameterizations are Brutsaert's (1975) model combined with Sicart et al.'s (2006) A cloud correction, Dilley and O'Brien's (1998) B model combined with Sicart et al.'s (2006) A cloud correction, and Dilley and O'Brien's (1998) A model combined with Sicart et al.'s

TABLE 5. All-sky parameterizations without the cloud factor used in this work. The variable q (g kg^{-1}) is the specific humidity, T (K) is the air temperature, and e (Pa) is the vapor pressure.

Source	Parameterization	Parameters	RMSE	MBE
Abramowitz et al. (2012)	$L_{in} = a + bT + ce$	$a = 0.2658$, $b = 0.7314$, c = 0.1519	26.5	0.35
Duguay (1993)	$L_{in} = \sigma T^4(a + be)$	$a = 0.6949$, $b = 0.000\,25$	23.6	−0.36
Mölg et al. (2008)	$L_{in} = a + bT + ce + dT^2 + fTe + he^2$	$a = 8565$, $b = -66.75$, $c = 3.1156$, $d = 0.1324$, $f = -0.011$, $h = 0.000\,08$	22	0
Naud et al. (2013)	$L_{in} = aq^b$	$a = 202.6$, $b = 0.2246$	26.3	0.04

(2006) A cloud correction (Table 8). The respective RMSEs are 28.2, 28.5, and 28.6 W m^{-2}, while the mean RMSE of all of the all-sky parameterizations is 31.9 W m^{-2}. The corresponding MBEs are 0.34, −0.2, and 0.03 W m^{-2}, respectively. The STDs of L_{in} for the three all-sky parameterizations are 39.1, 37.9, and 38.5 W m^{-2}, respectively, which are lower than that of the measurement value at AWS3-M (49.8 W m^{-2}). Relative to the control tests (recalibrated parameters for local conditions at AWS3-M), the RMSEb from spatial parameter transfer tests is 1.5 W m^{-2} smaller for the best three all-sky parameterizations.

AWS1-Z on Zhadang Glacier in the southern central TP is located far away from AWS1-M. Brutsaert's (1975) model combined with Sicart et al.'s (2006) B cloud correction, Dilley and O'Brien's (1998) A model combined with Sicart et al.'s (2006) A cloud correction, and Konzelmann et al.'s (1994) model combined with Sicart et al.'s (2006) B cloud correction are the best L_{in} models. The RMSEs of the three parameterizations are 33.8, 33.7, and 33.8 W m^{-2}, respectively. The respective MBEs are 0.1, 0.4, and 0.3 W m^{-2}. The corresponding STDs are 43.8, 42.2, and 43.3 W m^{-2}, respectively, which are roughly 8 W m^{-2} lower than that of the measured L_{in}. The difference in RMSEbs between the spatial parameter transfer tests and control tests (recalibrated parameters for local conditions at AWS1-Z) was less than 2.8 W m^{-2} for the best three all-sky parameterizations.

The last validation site is AWS2-P on Parlung 4 Glacier in the southeastern TP, which is the site farthest away from AWS1-M. The best four parameterizations are Brutsaert's (1975) model combined with Sicart et al.'s (2006) A cloud correction, Konzelmann et al.'s (1994) model combined with Sicart et al.'s (2006) A cloud correction, Dilley and O'Brien's (1998) A model combined with Sicart et al.'s (2006) A cloud correction, and Dilley and O'Brien's (1998) B model combined with Sicart et al.'s (2006) A cloud correction (Table 8). These all-sky parameterizations yield respective RMSEs of 29.4, 29.4, 29.2, and 29.2 W m^{-2}. The respective MBEs are −0.4, −0.5, −1.1, and −1.1 W m^{-2}. The STDs (46.4, 46, 47.3, and 47.3 W m^{-2}, respectively) of the modeled L_{in} do not agree well with the measured L_{in} (61.1 W m^{-2}). For the best four all-sky parameterizations, the difference in RMSEbs between spatial parameter transfer tests and control tests (recalibrated parameters for local conditions at AWS2-P) is ~(3.0–4.3) W m^{-2}, which is the largest for the five sites.

e. Summary

Based on the above analysis, the best all-sky parameterization for the five sites is Dilley and O'Brien's (1998) A model for clear-sky conditions combined with Sicart et al.'s (2006) A cloud correction with a mean RMSE of 26.3 W m^{-2} and a mean MBE of 0 W m^{-2}. The performance of Dilley and O'Brien's (1998) B model combined with Sicart et al.'s (2006) A cloud correction, Brutsaert's (1975) model combined with Sicart et al.'s (2006) A cloud correction, and Konzelmann et al.'s (1994) model combined with Sicart et al.'s (2006) A cloud correction is slightly worse than that of the best all-sky parameterization. The strong performance of these combinations may be attributable to good parameterizations of emissivity for cloudy conditions, which have been established for the high-mountain region.

The performance of parameter transferability in space presents spatial discrepancies. When the parameters are calibrated at AWS1-M in the Muztagata region, the parameter transferability in space performs much better in the northwestern TP than that in the southern TP. We also tested the performance of the best all-sky parameterization at the Ngari station for desert environment observation and research (NASDE) in the northwestern TP and in the Sergyemla Mountains in the southeastern TP (Fig. 1) using daily mean meteorological data downloaded from the Third Pole Environment database (http://www.tpedatabase.cn/). This verified our finding. The RMSE and MBE are 10.6 and 1.6 W m^{-2} at NASDE, respectively, for the measurement periods (from 3 December 2010 to 31 December 2013). The RMSE and MBE are 25.5 and −15.9 W m^{-2} in the Sergyemla Mountains, respectively, for the measurement periods (from 18 August 2005 to 24 December 2008). The modeled L_{in} is considerably underestimated in the Sergyemla Mountains. The AWS of the Sergyemla Mountains was located in the upper limits of fir forest,

TABLE 6. The RMSE (MBE) ($W m^{-2}$) of estimated L_{in} of all-sky conditions for the AWS1-M site obtained from each combination of cloud corrections and clear-sky algorithms for 2010.

Clear-sky parameterization	Cloud correction									
	KI	KA	KO	LH	MC	MA	MG	SA	SB	UM
CBR	19.4 (0.4)	25.1 (1.3)	19.7 (−0.5)	19 (−0.1)	19 (0.1)	19 (−0.1)	18.9 (−0.1)	19.1 (−0.2)	19.2 (−0.1)	19 (0.3)
CBT	19.2 (0.2)	25.1 (1.3)	19.7 (−0.6)	18.9 (−0.1)	18.9 (0)	19 (−0.1)	18.8 (−0.2)	19 (−0.2)	19.1 (−0.2)	18.9 (0.2)
CDOA	19.3 (0)	25.1 (1.3)	19.8 (−0.6)	19 (−0.3)	19 (−0.1)	19 (−0.1)	18.9 (−0.3)	19 (−0.3)	19.2 (−0.3)	19 (0.1)
CDOB	19.2 (0.1)	25.1 (1.3)	19.6 (−0.6)	18.8 (−0.2)	18.8 (−0.1)	19 (−0.1)	18.7 (−0.3)	18.9 (−0.3)	19 (−0.3)	18.8 (0.1)
CGA	19.2 (0.2)	25.1 (1.3)	19.8 (−0.5)	19 (−0.2)	19 (0)	19 (−0.1)	18.8 (−0.2)	19 (−0.2)	19.2 (−0.2)	19 (0.2)
CID	19.3 (1.2)	25.1 (1.3)	19.6 (−0.2)	19 (0.2)	19 (0.4)	19 (−0.1)	18.8 (0.2)	19.3 (0.2)	19.3 (0.2)	19 (0.9)
CIZ	19.5 (0.2)	25.3 (3.4)	19.9 (−0.6)	19.1 (−0.2)	19.1 (−0.1)	19 (−0.1)	19 (−0.2)	19.1 (−0.2)	19.3 (−0.2)	19.1 (0.2)
CKO	19.2 (0.2)	25.1 (1.3)	19.7 (−0.6)	18.9 (−0.1)	18.9 (0)	19 (−0.1)	18.8 (−0.2)	19 (−0.2)	19.1 (−0.2)	18.9 (0.2)
CNI	19.2 (0.2)	25.3 (3.4)	19.7 (−0.6)	18.9 (−0.1)	18.9 (0)	19 (−0.1)	18.8 (−0.2)	19 (−0.2)	19.1 (−0.1)	18.9 (0.2)
CPR	19.2 (0.4)	25.1 (1.3)	19.6 (−0.5)	18.9 (−0.1)	18.9 (0)	19 (−0.1)	18.8 (−0.2)	19.1 (−0.2)	19.1 (−0.2)	18.9 (0.3)

and the height of the air temperature sensor is about 3 m above ground (Liu and Luo 2011). The colder subcanopy (2 m) air temperature, because of the forest canopy acting as a cold sink for air, caused this underestimation for modeling L_{in} (Webster et al. 2016). Spatial discrepancies in parameter transferability in space may have resulted from different climatic conditions and the structure of the atmosphere (Swinbank 1964; Juszak and Pellicciotti 2013). To improve the performance of the model, recalibrated parameters of the all-sky parameterization based on local conditions are necessary, especially for regions that are influenced by different climate conditions on the TP.

In addition, the performance of parameter transferability in time is better than that of parameter transferability in space for the same all-sky parameterizations. The difference in RMSEbs for most all-sky parameterizations between temporal parameter transfer tests and the control test (calibrated coefficient at AWS1-M) is less than 0.5 $W m^{-2}$, and this difference is mainly derived from the MBE. The mean difference of RMSEbs of all the all-sky parameterizations between the temporal parameter transfer tests and the control tests at AWS1-M is roughly 5 $W m^{-2}$ lower than that between the spatial parameter transfer tests and the control tests (recalibrated coefficient for local conditions at AWSs) for the other four sites (Tables 6, 7, and 8).

5. Discussion

a. *Possible factors contributing to the RMSE distribution pattern of all-sky parameterization*

For parameter transferability in space, the higher the altitude is, the worse the performance of all-sky parameterizations is (Table 8). Even when the parameterizations are calibrated by local conditions for each site, the same results are produced. The RMSEb (or RMSE) of all-sky parameterizations increases with increasing altitude. This means that the performance of all-sky parameterizations decreases with increasing altitude. Several factors may help explain the spatial distribution of RMSEb (or the simulation ability) for all-sky parameterizations at different altitudes.

The first factor is the screen-level T/humidity. The L_{in} at the surface is mainly emitted by the entire layer within the first 1 km of the atmosphere (Ohmura 2001). However, the longwave radiation models tested are based on screen-level T/humidity and do not account for variabilities in the profiles of such parameters in the atmosphere. The differences between screen-level T/humidity and atmospheric profiles of T/humidity at various locations may cause differences in model performance, especially for differences between screen-level T and atmospheric profiles of T. The sensitivity of L_{in} against changes in the temperature profile (4 $W m^{-2} K^{-1}$) is more significant than the sensitivity of L_{in} against changes in the humidity profile (0.55 $W m^{-2}$ $\%^{-1}$) (Viúdez-Mora et al. 2009). The effective atmospheric boundary layer (ABL) temperature that depends directly on profiles of T/humidity is derived from radiation emitted by atmospheric water vapor in the ABL and is a powerful indicator for the state of the ABL (Gröbner et al. 2009). The gap between screen-level T and the effective ABL temperature is different at different altitudes (Gröbner et al. 2009). Relative to parameterizations that use screen-level T/humidity data only, parameterizations with an effective ABL temperature or effective radiating temperature can obtain better estimations of L_{in} (Gröbner et al. 2009; Wacker et al. 2014). Thus, parameterization performance decreases with an increasing difference between the effective ABL temperature and screen-level T. The difference between the effective ABL temperature and screen-level T is larger at higher-altitude sites

TABLE 7. The RMSEb for all-sky parameterizations with calibrated coefficients for 2010 (recalibrated coefficients of the observation period except for 2010) for the AWS1-M site.

Clear-sky parameterization	Cloud correction									
	KI	KA	KO	LH	MC	MA	MG	SA	SB	UM
CBR	20.9 (20.2)	28.3 (26.2)	21 (21)	20.2 (20.6)	20.4 (20.7)	20.2 (20.2)	20.2 (20.5)	20.6 (20.8)	20.4 (20.8)	20.7 (20.3)
CBT	20.4 (20.2)	28.3 (26.2)	20.8 (21)	20.2 (20.5)	20.3 (20.6)	20.2 (20.2)	20.1 (20.4)	20.6 (20.6)	20.3 (20.6)	20.5 (20.2)
CDOA	20.6 (20.4)	28.3 (26.2)	21 (21.1)	20.3 (20.7)	20.4 (20.8)	20.2 (20.2)	20.3 (20.6)	20.8 (20.8)	20.5 (20.8)	20.7 (20.2)
CDOB	20.6 (20.2)	28.3 (26.2)	20.8 (21)	20.1 (20.5)	20.3 (20.6)	20.2 (20.2)	20.1 (20.5)	20.6 (20.6)	20.4 (20.7)	20.5 (20)
CGA	20.9 (20.4)	28.3 (26.2)	21.2 (21.1)	20.7 (20.8)	20.8 (20.8)	20.2 (20.2)	20.6 (20.7)	20.5 (20.5)	20.4 (20.9)	21.1 (20.4)
CID	21.4 (20.9)	28.3 (26.2)	20.9 (20.6)	20.2 (20.1)	20.3 (20.2)	20.2 (20.2)	20.1 (19.9)	20.5 (20.3)	20.4 (20.3)	21 (20.9)
CIZ	20.4 (20.3)	30.7 (28.7)	20.7 (21.1)	20.1 (20.6)	20 (20.8)	20.2 (20.2)	20 (20.6)	20.9 (20.8)	20.6 (20.8)	20.3 (20.2)
CKO	20.4 (20.2)	28.3 (26.2)	20.8 (21)	20.2 (20.5)	20.3 (20.6)	20.2 (20.2)	20.1 (20.4)	20.6 (20.6)	20.3 (20.6)	20.5 (20.2)
CNI	20.5 (20.2)	30.7 (28.7)	20.8 (21)	20.2 (20.5)	20.3 (20.6)	20.2 (20.2)	20.1 (20.4)	20.6 (20.6)	20.3 (20.6)	20.5 (20.2)
CPR	20.8 (20.1)	28.3 (26.2)	20.8 (21)	20.2 (20.6)	20.3 (20.7)	20.2 (20.2)	20.1 (20.5)	20.6 (20.8)	20.3 (20.8)	20.7 (20.3)

than at low ones [see Table 2 in Gröbner et al.'s (2009) paper]. This means that the screen-level T is more similar to the effective ABL temperature in lower-altitude sites. Therefore, the screen-level T/humidity contributes to the better performance of parameterizations for lower sites. The smaller difference between the screen-level T and effective ABL temperature for low-altitude sites may result from stronger turbulent exchanges in low-altitude sites than that in high-altitude sites.

The cloud-base height (CBH) is an another important factor. The CBH that is linked to cloud type determines the cloud emission temperature and air layers contributing to L_{in} that reach the surface. The cloud radiative effect, which is defined as the change in L_{in} at the surface when clouds are present relative to cloud-free conditions, decreases with increasing CBH at a rate of $5\,W\,m^{-2}\,km^{-1}$ during cold seasons and $4\,W\,m^{-2}\,km^{-1}$ during warm seasons (Viúdez-Mora et al. 2015). This means that L_{in} is influenced more by clouds at high-altitude sites than by clouds in lower sites because of higher CBH in lower sites. Other variables related to clouds, such as cloud height and temperature; cloud type, haze, and turbidity; and daily cloud cycles, also contribute to L_{in}. Because of the short horizontal distances and small difference in S_{in} that indicate minor differences in atmospheric optical thickness among the three AWSs, we can assume that these variables (e.g., cloud height and temperature; cloud type, haze, and turbidity; etc.) are the same for the three AWSs in the Muztagata region. However, the CBH clearly varies greatly at the three AWSs in the Muztagata region. As compared with the low-altitude sites, the land surface of high-altitude sites is close to the cloud base and is more heavily influenced by cloud cover. This process is not considered in a simple L_{in} model. Therefore, the L_{in} model performs less well for higher-altitude sites.

However, the distribution of larger RMSE values in higher-altitude sites is not constant. It can be refigured by factors such as terrain, underlying surfaces, wind systems, and so on. Terrain-emitted radiation is an important component of measured L_{in} when the mean elevation angle of the surrounding terrain is larger than 20° (Plüss and Ohmura 1997). This means that all-sky parameterizations without coupling with terrain-emitted radiation perform worse for steep slopes than for gentle slopes. The different underlying surfaces (e.g., snow surface) and/or wind systems (e.g., glacier wind) at two neighboring sites present a discrepancy between screen-level T/humidity regimes and temperature lapse rates, worsening the parameter transferability in space for neighboring sites (Juszak and Pellicciotti 2013).

b. L_{in} comparison with other sites on the TP

To compare L_{in} values, we collected published L_{in} data for the TP (Table 9 and Fig. 1). The reported mean L_{in} values focus on the warm season (from May to September). The objective of our comparison is to detect possible spatial characteristics of L_{in} on the TP and its driving factors.

The characteristics of L_{in} at different altitudes but in the same study region are analyzed. At different altitudes in the Muztagata region, the highest mean L_{in} is found at AWS1-M, while the lowest is found at AWS3-M for the same period (Table 9). The quantity L_{in} shows a significant degree of altitude dependence with a mean lapse rate of $-3.3\,W\,m^{-2}\,(100\,m)^{-1}$ for September 2011 to July 2013. Seasonal gradients varied from $-1.58\,W\,m^{-2}\,(100\,m)^{-1}$ in the winter to $-3.44\,W\,m^{-2}\,(100\,m)^{-1}$ in the summer. The L_{in} gradient is also found in other regions. Marty et al. (2002) found that the mean annual L_{in} decreased by $2.9\,W\,m^{-2}\,(100\,m)^{-1}$ between 370 and 3580 m MSL in the Swiss Alps. MacDonell et al. (2013) found that the mean

TABLE 8. The RMSEb for all-sky parameterizations with calibrated coefficients for 2010 at AWS1-M (recalibrated coefficients under local conditions) for the observation period at the four sites.

Clear-sky parameterization	Cloud correction									
	KI	KA	KO	LH	MC	MA	MG	SA	SB	UM
AWS2-M										
CBR	34.2 (31.9)	48.2 (35.1)	39.7 (33.4)	33.2 (27)	33.4 (29)	33.2 (27.1)	32.6 (26.3)	29 (25.4)	30.4 (26.7)	33.5 (31.6)
CBT	32.4 (31.6)	47.8 (35.1)	38.7 (33.3)	32.2 (26.9)	32.4 (28.7)	33.2 (27.1)	31.6 (26.2)	28.1 (25)	29.6 (26.5)	31.6 (31.4)
CDOA	32.8 (32.2)	47.9 (35.1)	39.1 (33.3)	32.4 (27.4)	32.5 (29.3)	33.2 (27.1)	31.8 (26.7)	27.9 (25.5)	29.6 (27)	32.4 (32)
CDOB	33.1 (32)	47.9 (35.1)	39.1 (33.2)	32.3 (27.1)	32.4 (29)	33.2 (27.1)	31.7 (26.4)	28.1 (25.4)	29.4 (26.7)	32.5 (31.7)
CGA	33.4 (31.7)	48.3 (35.1)	39.7 (33.3)	33.4 (27.3)	33.6 (29.1)	33.2 (27.1)	32.8 (26.7)	29 (25.1)	30.6 (27)	33 (31.7)
CID	36.4 (31.7)	48.8 (35.1)	40.3 (33.7)	34.5 (27)	34.7 (28.6)	33.2 (27.1)	33.9 (26.4)	31.4 (25.3)	31.9 (26.8)	35.1 (31.5)
CIZ	30.7 (32)	42 (35.1)	33 (33.5)	31.7 (27.1)	31.4 (29.1)	33.2 (27.1)	31.1 (26.4)	33.7 (25.7)	33.8 (26.8)	30.9 (31.7)
CKO	32.6 (31.6)	47.8 (43.7)	38.8 (33.3)	32.3 (26.9)	32.5 (28.7)	33.2 (27.1)	31.7 (26.2)	28.2 (25)	29.6 (26.5)	31.8 (31.4)
CNI	33.5 (32.2)	47.8 (43.7)	39.3 (33.5)	32.6 (27.4)	32.7 (29.4)	33.2 (27.1)	32 (26.7)	28.2 (25.9)	29.8 (27.1)	32.8 (32)
CPR	33.7 (31.7)	48.1 (35.1)	39.3 (33.3)	32.9 (26.8)	33 (28.8)	33.2 (27.1)	32.3 (26.1)	28.9 (25.4)	30.2 (26.5)	33 (31.5)
AWS3-M										
CBR	34.9 (35.6)	56.9 (37.5)	42.7 (35.4)	34 (29.1)	34.2 (30.6)	34 (29.4)	33.3 (28.3)	30.4 (27.6)	31.6 (28.5)	34.2 (35.3)
CBT	32.1 (35.3)	56.9 (37.5)	41 (35.4)	31.9 (29.1)	32.1 (30.2)	34 (29.4)	31.3 (28.2)	28.5 (26.8)	29.7 (28.5)	31 (35)
CDOA	32.3 (36.1)	56.9 (37.5)	41.2 (35.4)	31.8 (29.5)	32 (31)	34 (29.4)	31.2 (28.6)	28.7 (27.6)	30 (28.9)	31.8 (35.8)
CDOB	32.9 (36)	56.9 (37.5)	41.4 (35.4)	32 (29.3)	32.2 (30.8)	34 (29.4)	31.4 (28.4)	28.6 (27.5)	29.7 (28.7)	32.2 (35.6)
CGA	33.7 (35.6)	56.9 (37.5)	42.4 (35.5)	33.7 (29.5)	33.9 (30.6)	34 (29.4)	33.1 (28.6)	30 (26.9)	31.4 (28.8)	33.1 (35.4)
CID	38.8 (35.1)	56.9 (37.5)	44.6 (35.6)	37 (29)	37.3 (30.2)	34 (29.4)	36.4 (28.2)	34.1 (27.6)	34.7 (28.5)	37.6 (34.8)
CIZ	41.3 (35.6)	56.9 (37.5)	36.9 (35.4)	43.1 (29.2)	42.9 (30.7)	34 (29.4)	42.4 (28.3)	44.4 (28)	45.1 (28.6)	42 (35.3)
CKO	32.4 (35.3)	57.8 (43.6)	41.2 (35.4)	32.1 (29.1)	32.3 (30.2)	34 (29.4)	31.5 (28.2)	28.7 (26.9)	29.9 (28.4)	31.3 (35)
CNI	33.9 (35.7)	57.8 (43.6)	42.1 (35.5)	33.1 (29.4)	33.3 (30.6)	34 (29.4)	32.5 (28.5)	29.5 (27.2)	30.8 (28.7)	33.3 (35.5)
CPR	34.3 (35.4)	56.9 (37.5)	42.3 (35.4)	33.5 (28.9)	33.7 (30.3)	34 (29.4)	32.9 (28)	30.1 (27.4)	31.2 (28.3)	33.6 (35)
AWS1-Z										
CBR	38.5 (45.5)	53.3 (36.7)	41.9 (39.2)	38.7 (31.6)	38.7 (36.5)	38.7 (31.4)	38.4 (31.4)	35.3 (32)	35 (31.7)	38.9 (45.8)
CBT	36.9 (45.1)	53.3 (36.7)	40.7 (39)	37.5 (31.2)	37.6 (36)	38.7 (31.4)	37.3 (30.9)	34.4 (31.6)	33.9 (31.4)	37.2 (45.4)
CDOA	36.7 (45.2)	53.3 (36.7)	40.8 (38.8)	37.2 (31.7)	37.3 (36.3)	38.7 (31.4)	37 (31.5)	34.1 (32.1)	34.5 (32)	37.2 (45.4)
CDOB	37.2 (45.2)	53.3 (36.7)	40.9 (38.8)	37.5 (31.6)	37.5 (36.3)	38.7 (31.4)	37.3 (31.4)	34.3 (32.1)	34.2 (32)	37.6 (45.3)
CGA	38.1 (45.2)	53.3 (36.7)	41.9 (39)	38.9 (31.5)	39 (36.3)	38.7 (31.4)	38.7 (31.2)	35.6 (31.9)	35.2 (31.7)	38.8 (45.4)
CID	42.2 (45.6)	53.3 (36.7)	43.9 (39.5)	41.7 (31.5)	41.8 (36.6)	38.7 (31.4)	41.4 (31.2)	37.9 (31.7)	38 (31.7)	42.2 (46)
CIZ	48.9 (45.7)	53.3 (36.7)	43.3 (39.3)	51.3 (31.9)	51.1 (36.8)	38.7 (31.4)	51.1 (31.6)	40.8 (32.1)	59.7 (31.9)	50.1 (46)
CKO	37.1 (45.2)	55.1 (45.6)	40.8 (39)	37.7 (31.2)	37.7 (36.1)	38.7 (31.4)	37.4 (31)	34.5 (31.6)	34.1 (31.4)	37.4 (45.5)
CNI	37.1 (45.3)	55.1 (45.6)	40.9 (39)	37.3 (31.5)	37.3 (36.3)	38.7 (31.4)	37 (31.3)	34.2 (32)	34.2 (31.7)	37.5 (45.5)
CPR	38.4 (45.4)	53.3 (36.7)	41.7 (39.1)	38.6 (31.5)	38.7 (36.4)	38.7 (31.4)	38.4 (31.3)	35.2 (31.9)	35 (31.7)	38.8 (45.8)
AWS2-P										
CBR	35 (38.6)	42.9 (39.5)	37.4 (34.8)	36 (30.1)	36.2 (30.9)	35.9 (30.1)	35.2 (29.6)	30.9 (27)	33.8 (28.5)	36.1 (38)
CBT	35.3 (38.8)	42.9 (39.5)	37.8 (35)	36.6 (30.3)	36.9 (30.6)	35.9 (30.1)	36 (29.8)	29.8 (26.3)	32.8 (28.7)	36.7 (38.4)
CDOA	34.5 (37.8)	42.9 (39.5)	37 (34.8)	35.7 (30)	35.9 (30.1)	35.9 (30.1)	34.9 (29.6)	30.3 (26)	34 (28.5)	35.8 (37.5)
CDOB	34.6 (37.1)	42.9 (39.5)	37 (34.6)	35.7 (29.5)	35.9 (29.6)	35.9 (30.1)	35 (29.1)	30.3 (26.1)	33.3 (28.1)	35.8 (36.9)
CGA	35.1 (38.7)	42.9 (39.5)	37.5 (34.8)	36.4 (30.2)	36.7 (30.9)	35.9 (30.1)	35.7 (29.7)	30.6 (27.1)	33.1 (28.6)	36.5 (38.1)
CID	37.1 (36.8)	42.9 (39.5)	38.9 (34.2)	37.8 (29.1)	38.3 (30)	35.9 (30.1)	37.3 (28.8)	30.6 (27.2)	30.7 (27.9)	38.1 (36.4)
CIZ	38.8 (38.3)	42.9 (39.5)	35.9 (34.6)	37.8 (29.9)	37.7 (30.9)	35.9 (30.1)	38.4 (29.5)	43.6 (27.4)	45.8 (28.6)	37.5 (37.7)
CKO	35.3 (38.7)	43.5 (48.1)	37.8 (34.9)	36.6 (30.2)	36.9 (30.6)	35.9 (30.1)	35.9 (29.7)	30 (26.4)	32.8 (28.6)	36.6 (38.2)
CNI	34.8 (38.4)	43.5 (48.1)	37.4 (34.6)	35.8 (29.9)	36 (30.9)	35.9 (30.1)	35.1 (29.5)	30.5 (27.3)	34 (28.6)	35.9 (37.7)
CPR	35.3 (38.7)	42.9 (39.5)	37.6 (34.9)	36.3 (30.2)	36.6 (30.6)	35.9 (30.1)	35.7 (29.8)	30.6 (26.4)	32.8 (28.6)	36.5 (38.2)

annual L_{in} decreased by $8\,W\,m^{-2}$ $(100\,m)^{-1}$ in the Chilean Andes.

Marty et al. (2002) believed that the above results could be explained by changes in temperature and moisture content with elevation in the atmospheric column. In the Muztagata region, the T and e gradients are $-6.6°C\,(1000\,m)^{-1}$ and $-0.8\,Pa\,(100\,m)^{-1}$. However, RH is almost constant at different altitudes (Table 9), and the distribution of e is controlled by T in the Muztagata region. Thus, the T gradient is the main factor that decreases L_{in} with increasing altitude in the Muztagata region.

The spatial distributions of L_{in} on the TP were analyzed by collecting measurement data (Fig. 1). The L_{in} value for the Muztagata region is smaller than that for high-altitude environments (close to or on glaciers) in the southern TP for the warm season (from May to September) at comparable altitudes (Table 9). A lower L_{in} value was also found for Laohugou 12 Glacier on the northeastern TP and in the NASDE for the

TABLE 9. Meteorological data and L_{in} collected from different sites on or near glaciers on the TP. Three regions are defined in Yao et al. (2013).

	Sites	Period	Alt (m)	T (°C)	RH (%)	L_{in} (W m^{-2})	S_{in} (W m^{-2})	
South Asian monsoon	East Rongbuk	May–Jul 2005	6560	−6.7	66.6	221		X. Yang et al. (2010)
	Sergyemla Mountains	May–Sep 2008	4430	6.6	86	332	191	This study
	Parlung 4	May–Sep 2009	4800	3.7	78.5	295	242	Yang et al. (2011)
		May–Sep 2012		2.6	80	296	209	This study
	Zhadang	May–Sep 2009	5665	1.2	70.4	255	264	Zhang et al. (2013)
		May–Sep 2010		0.6	69.9	258	274	
		May–Sep 2012		2.6	80	296	209	This study
	Chhota Shigri	Jun 2010–Sep 2013	4863	2.5	68	289	266	Azam et al. (2014)
		Jun–Sep 2013	4670	3.6	82	300	248	Azam et al. (2014)
Transition	NASDE	May–Sep 2011	4262	11.6	31	289	285	This study
		May–Sep 2012		11.3	30.9	287	325	This study
Westerlies	Qiyi	May–Sep 2003	4295	1.2	59.8	279	222	Sakai et al. (2006)
	Laohugou 12	May–Sep 2009	5040	−3.7	61.4	226	261	Sun et al. (2011)
	AWS1-M	May–Sep 2010	3655	7.6	57.1	295	262	This study
		May–Sep 2011		9.1	47	289	288	
		May–Sep 2012		7.4	56.3	295	267	
		May–Sep 2013		8.9	46.2	288	285	
	AWS2-M	May–Sep 2012	4400	2.1	60.2	268	270	
		May–Sep 2013		3.9	46	264	293	
	AWS3-M	May–Sep 2012	4900	−1.4	63.7	253	279	

northwestern TP. Above all, L_{in} is smaller in the northern TP than that in the southern TP at the same altitudes.

The spatial distribution of L_{in} on the TP is related to the T, RH, and cloud cover. The impact of cloud cover on L_{in} is minor for both the winter and summer on the TP (Naud et al. 2015). Moreover, as few cloud cover data are available for the TP, we only analyze the influence of T and RH on the spatial distribution of L_{in}. The quantity L_{in} is strongly positively correlated with T based on our statistical analysis of the collected data (Fig. 3). The slope coefficient is larger in the monsoon region than that for the westerlies region of the TP, meaning that L_{in} is more sensitive to T in moist areas than in arid areas. This may be attributable to the higher humidity and cloud cover in the monsoon region. A correlation between L_{in} and RH is evident in the monsoon region of the TP, especially in the southeastern TP (Table 2 and Fig. 3). However, this correlation is not obvious in the northern TP (Fig. 3). Therefore, the spatial distribution of L_{in} may be driven by T on the TP. However, L_{in} is also driven by moisture in the southern TP where more warm moist air exists through the South Asian monsoon in addition to T.

6. Conclusions

Data drawn from AWSs installed in the Muztagata region and on Zhadang and Parlung 4 Glaciers allowed us to test 13 parameterizations of clear-sky atmospheric emissivity combined with 10 cloud corrections for estimating L_{in} for all-sky conditions in regions presenting different TP climates through temporal and spatial parameter transfer tests. The main conclusions are described here.

Most locally calibrated parameterizations for clear-sky and all-sky conditions perform well when applied to the calibration site. For the five sites, the best all-sky parameterization is Dilley and O'Brien's (1998) A model for clear-sky conditions combined with Sicart et al.'s (2006) A cloud-correction-incorporated RH. The performance of Dilley and O'Brien's (1998) B model combined with Sicart et al.'s (2006) A cloud correction, Brutsaert's (1975) model combined with Sicart et al.'s (2006) A cloud correction, and Konzelmann et al.'s (1994) model combined with Sicart et al.'s (2006) A cloud correction is slightly worse than the best all-sky parameterization. When the parameters are calibrated at AWS1-M for the Muztagata region, the all-sky parameterization produces better results at AWSs in the northwestern TP than that for the other two AWSs in the southern TP, suggesting that this calibrated model is more robust for the northwestern TP. Recalibrated parameters of the all-sky parameterizations based on local conditions are necessary for improving the performance of the models on the TP. The performance of parameter transferability in time is better than that in space for the same all-sky parameterizations.

The performance of all all-sky parameterizations decreases with increasing altitude on the TP, whether parameters of all-sky parameterizations are recalibrated

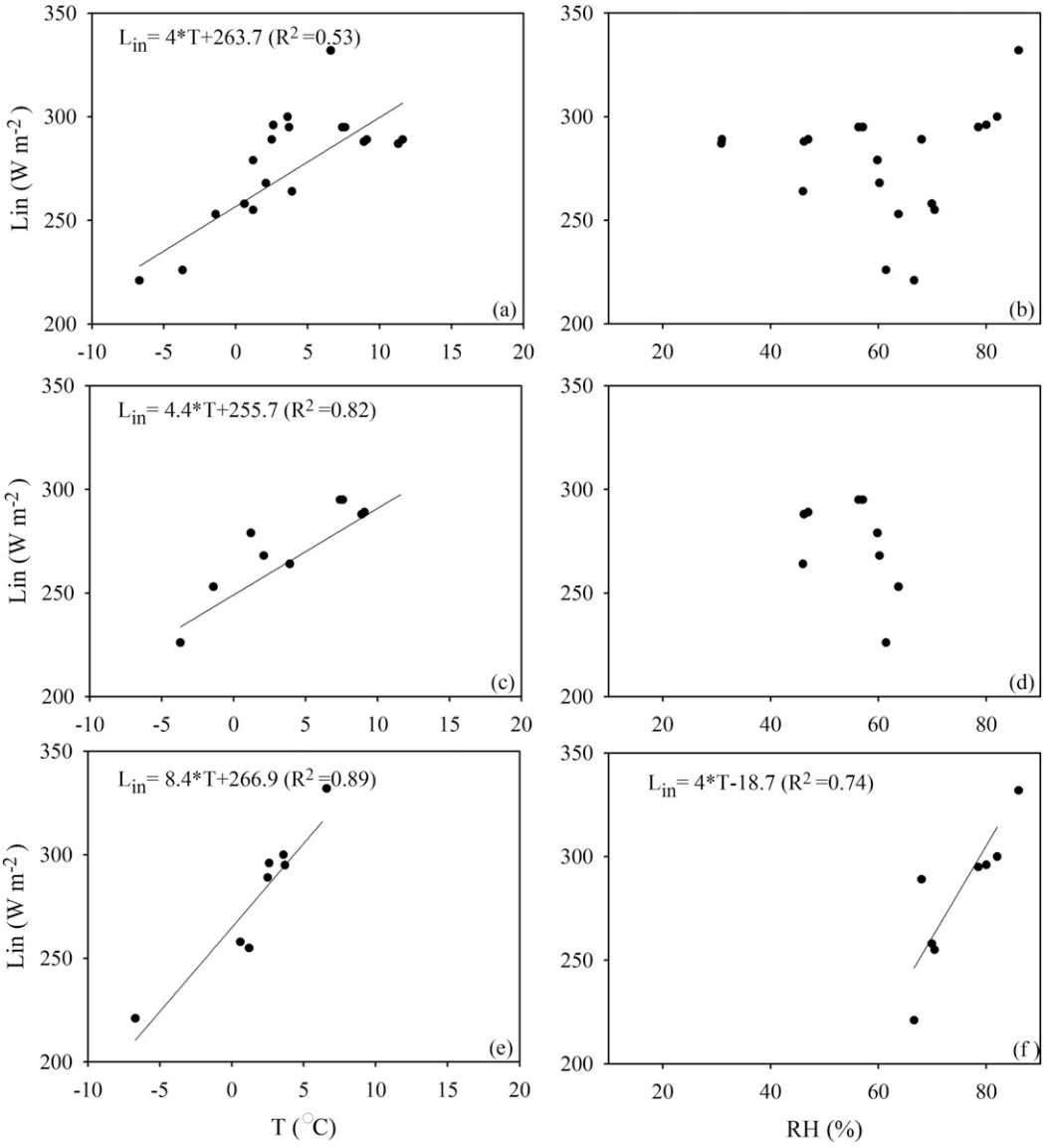

FIG. 3. The L_{in} vs (left) T and (right) RH, along with the linear fits between L_{in} and T or RH, for (a),(b) all of the data on the TP or with a focus on the data from regions mainly controlled by (c),(d) westerlies or (e),(f) the South Asian monsoon.

by local conditions in different locations or are transferred from AWS1-M. This may be attributed to the difference between screen-level T and the effective ABL temperature and to different cloud-base heights at different altitudes. The distribution of larger RMSE values at higher altitudes is likely to be refigured by terrain, underlying surfaces, wind systems, and so on.

In the Muztagata region, L_{in} shows a significant degree of altitude dependence with a mean lapse rate of $-3.3\,W\,m^{-2}\,(100\,m)^{-1}$ from September 2011 to July 2013. In addition, L_{in} is found to be smaller in the northern TP than that in the southern TP at the same altitudes by analyzing results from the few studies that have been conducted on L_{in} for the mountain regions of the TP. The spatial distribution of L_{in} may be driven by T on the TP. In the southern TP, L_{in} is also driven by moisture in addition to T.

Subsequent works will focus on using data from these monitoring stations and distributed energy–mass balance models to investigate the mechanisms responsible for spatially heterogeneous changes of Tibetan glaciers. In addition, the best all-sky parameterization can be used to produce a longer L_{in} record and to fill data gaps for the high-mountain regions of the TP according to

meteorological data collected from AWSs, thereby allowing for the long-term calculation of energy and mass balances for glacial surfaces.

Acknowledgments. We acknowledge the staff at Muztagh Ata Station for Westerly Environment Observation and Research and at Nam Co Monitoring and Research Station for Multisphere Interactions, Institute of Tibetan Research, Chinese Academy of Sciences, for help in the field. We thank reviewers and the editor, Paquita Zuidema, for valuable insights that greatly strengthened the manuscript. We thank the Third Pole Environment database, Institute of Tibetan Research, Chinese Academy of Sciences and National Climate Center, China Meteorological Administration, for providing the climate data used herein. This study was jointly funded by National Natural Science Foundation of China (Grant 41190081), the China National Funds for Distinguished Young Scientists 41125003, and the National Natural Science Foundation of China (Grants 91547104, 41371085, 40901047, and 41601081).

REFERENCES

Abramowitz, G., L. Pouyanné, and H. Ajami, 2012: On the information content of surface meteorology for downward atmospheric long-wave radiation synthesis. *Geophys. Res. Lett.*, **39**, L04808, doi:10.1029/2011GL050726.

Alados, I., I. Foyo-Moreno, and L. Alados-Arboledas, 2012: Estimation of downwelling longwave irradiance under all-sky conditions. *Int. J. Climatol.*, **32**, 781–793, doi:10.1002/joc.2307.

Azam, M. F., P. Wagnon, C. Vincent, A. L. Ramanathan, V. Favier, A. Mandal, and J. G. Pottakkal, 2014: Processes governing the mass balance of Chhota Shigri Glacier (western Himalaya, India) assessed by point-scale surface energy balance measurements. *Cryosphere*, **8**, 2195–2217, doi:10.5194/tc-8-2195-2014.

Brunt, D., 1932: Notes on radiation in the atmosphere. *Quart. J. Roy. Meteor. Soc.*, **58**, 389–420, doi:10.1002/qj.49705824704.

Brutsaert, W., 1975: On a derivable formula for long-wave radiation from clear skies. *Water Resour. Res.*, **11**, 742–744, doi:10.1029/WR011i005p00742.

Carmona, F., R. Rivas, and V. Caselles, 2014: Estimation of daytime downward longwave radiation under clear and cloudy skies conditions over a sub-humid region. *Theor. Appl. Climatol.*, **115**, 281–295, doi:10.1007/s00704-013-0891-3.

Crawford, T. M., and C. E. Duchon, 1999: An improved parameterization for estimating effective atmospheric emissivity for use in calculating daytime downwelling longwave radiation. *J. Appl. Meteor.*, **38**, 474–480, doi:10.1175/1520-0450(1999)038<0474:AIPFEE>2.0.CO;2.

Dilley, A. C., and D. M. O'Brien, 1998: Estimating downward clear sky long-wave irradiance at the surface from screen temperature and precipitable water. *Quart. J. Roy. Meteor. Soc.*, **124**, 1391–1401, doi:10.1002/qj.49712454903.

Duguay, C. R., 1993: Radiation modeling in mountainous terrain review and status. *Mt. Res. Dev.*, **13**, 339–357.

Flerchinger, G. N., W. Xaio, D. Marks, T. J. Sauer, and Q. Yu, 2009: Comparison of algorithms for incoming atmospheric longwave radiation. *Water Resour. Res.*, **45**, W03423, doi:10.1029/2008WR007394.

Gardelle, J., E. Berthier, and Y. Arnaud, 2012: Slight mass gain of Karakoram glaciers in the early twenty-first century. *Nat. Geosci.*, **5**, 322–325, doi:10.1038/ngeo1450.

Garratt, J. R., 1992: Extreme maximum land surface temperatures. *J. Appl. Meteor.*, **31**, 1096–1105, doi:10.1175/1520-0450(1992)031<1096:EMLST>2.0.CO;2.

Greuell, W., W. H. Knap, and P. C. Smeets, 1997: Elevational changes in meteorological variables along a midlatitude glacier during summer. *J. Geophys. Res.*, **102**, 25 941–25 954, doi:10.1029/97JD02083.

Gröbner, J., S. Wacker, L. Vuilleumier, and N. Kämpfer, 2009: Effective atmospheric boundary layer temperature from longwave radiation measurements. *J. Geophys. Res.*, **114**, D19116, doi:10.1029/2009JD012274.

Gubler, S., S. Gruber, and R. S. Purves, 2012: Uncertainties of parameterized surface downward clear-sky shortwave and all-sky longwave radiation. *Atmos. Chem. Phys.*, **12**, 5077–5098, doi:10.5194/acp-12-5077-2012.

Idso, S. B., 1981: A set of equations for full spectrum and 8- to 14-μm and 10.5- to 12.5-μm thermal radiation from cloudless skies. *Water Resour. Res.*, **17**, 295–304, doi:10.1029/WR017i002p00295.

——, and R. D. Jackson, 1969: Thermal radiation from the atmosphere. *J. Geophys. Res.*, **74**, 5397–5403, doi:10.1029/JC074i023p05397.

Iziomon, M. G., H. Mayer, and A. Matzarakis, 2003: Downward atmospheric longwave irradiance under clear and cloudy skies: Measurement and parameterization. *J. Atmos. Sol.-Terr. Phys.*, **65**, 1107–1116, doi:10.1016/j.jastp.2003.07.007.

Juszak, I., and F. Pellicciotti, 2013: A comparison of parameterizations of incoming longwave radiation over melting glaciers: Model robustness and seasonal variability. *J. Geophys. Res. Atmos.*, **118**, 3066–3084, doi:10.1002/jgrd.50277.

Kasten, F., and G. Czeplak, 1980: Solar and terrestrial radiation dependent on the amount and type of cloud. *Sol. Energy*, **24**, 177–189, doi:10.1016/0038-092X(80)90391-6.

Kimball, B. A., S. B. Idso, and J. K. Aase, 1982: A model of thermal radiation from partly cloudy and overcast skies. *Water Resour. Res.*, **18**, 931–936, doi:10.1029/WR018i004p00931.

Klok, E. J. L., and J. Oerlemans, 2002: Model study of the spatial distribution of the energy and mass balance of Morteratschgletscher, Switzerland. *J. Glaciol.*, **48**, 505–518, doi:10.3189/172756502781831133.

König-Langlo, G., and E. Augstein, 1994: Parameterization of the downward long-wave radiation at the Earth's surface in polar regions. *Meteor. Z.*, **3**, 343–347.

Konzelmann, T., R. S. W. van de Wal, W. Greuell, R. Bintanja, E. A. C. Henneken, and A. Abe-Ouchi, 1994: Parameterization of global and longwave incoming radiation for the Greenland ice sheet. *Global Planet. Change*, **9**, 143–164, doi:10.1016/0921-8181(94)90013-2.

Kuipers Munneke, P., C. H. Reijmer, and M. R. van den Broeke, 2011: Assessing the retrieval of cloud properties from radiation measurements over snow and ice. *Int. J. Climatol.*, **31**, 756–769, doi:10.1002/joc.2114.

Lhomme, J. P., J. J. Vacher, and A. Rocheteau, 2007: Estimating downward long-wave radiation on the Andean Altiplano. *Agric. For. Meteor.*, **145**, 139–148, doi:10.1016/j.agrformet.2007.04.007.

Liu, X., and T. Luo, 2011: Spatiotemporal variability of soil temperature and moisture across two contrasting timberline ecotones in the Sergyemla Mountains, southeast Tibet. *Arct. Antarct. Alp. Res.*, **43**, 229–238, doi:10.1657/1938-4246-43.2.229.

MacDonell, S., L. Nicholson, and C. Kinnard, 2013: Parameterisation of incoming longwave radiation over glacier surfaces in the semiarid Andes of Chile. *Theor. Appl. Climatol.*, **111**, 513–528, doi:10.1007/s00704-012-0675-1.

Marshunova, M. S., 1966: Principal characteristics of the radiation balance of the underlying surface. Soviet data on the Arctic heat budget and its climate influence, Rand Corp. Rep. R. M. 5003-PR, 51–132.

Marthews, T., Y. Malhi, and H. Iwata, 2012: Calculating downward longwave radiation under clear and cloudy conditions over a tropical lowland forest site: An evaluation of model schemes for hourly data. *Theor. Appl. Climatol.*, **107**, 461–477, doi:10.1007/s00704-011-0486-9.

Marty, C., and R. Philipona, 2000: The clear-sky index to separate clear-sky from cloudy-sky situations in climate research. *Geophys. Res. Lett.*, **27**, 2649–2652, doi:10.1029/2000GL011743.

——, ——, C. Fröhlich, and A. Ohmura, 2002: Altitude dependence of surface radiation fluxes and cloud forcing in the Alps: Results from the alpine surface radiation budget network. *Theor. Appl. Climatol.*, **72**, 137–155, doi:10.1007/s007040200019.

Maykut, G. A., and P. E. Church, 1973: Radiation climate of Barrow Alaska, 1962–66. *J. Appl. Meteor.*, **12**, 620–628, doi:10.1175/1520-0450(1973)012<0620:RCOBA>2.0.CO;2.

Mölg, T., N. J. Cullen, D. R. Hardy, G. Kaser, and L. Klok, 2008: Mass balance of a slope glacier on Kilimanjaro and its sensitivity to climate. *Int. J. Climatol.*, **28**, 881–892, doi:10.1002/joc.1589.

——, ——, and G. Kaser, 2009: Solar radiation, cloudiness and longwave radiation over low-latitude glaciers: Implications for mass-balance modelling. *J. Glaciol.*, **55**, 292–302, doi:10.3189/002214309788608822.

Naud, C. M., Y. Chen, I. Rangwala, and J. R. Miller, 2013: Sensitivity of downward longwave surface radiation to moisture and cloud changes in a high-elevation region. *J. Geophys. Res. Atmos.*, **118**, 10 072–10 081, doi:10.1002/jgrd.50644.

——, I. Rangwala, M. Xu, and J. R. Miller, 2015: A satellite view of the radiative impact of clouds on surface downward fluxes in the Tibetan Plateau. *J. Appl. Meteor. Climatol.*, **54**, 479–493, doi:10.1175/JAMC-D-14-0183.1.

Niemelä, S., P. Räisänen, and H. Savijärvi, 2001: Comparison of surface radiative flux parameterisations: Part I: Longwave radiation. *Atmos. Res.*, **58**, 1–18, doi:10.1016/S0169-8095(01)00084-9.

Ohmura, A., 2001: Physical basis for the temperature-based melt-index method. *J. Appl. Meteor.*, **40**, 753–761, doi:10.1175/1520-0450(2001)040<0753:PBFTTB>2.0.CO;2.

Philipona, R., B. Dürr, A. Ohmura, and C. Ruckstuhl, 2005: Anthropogenic greenhouse forcing and strong water vapor feedback increase temperature in Europe. *Geophys. Res. Lett.*, **32**, L19809, doi:10.1029/2005GL023624.

Plüss, C., and A. Ohmura, 1997: Longwave radiation on snow-covered mountainous surfaces. *J. Appl. Meteor.*, **36**, 818–824, doi:10.1175/1520-0450-36.6.818.

Prata, A. J., 1996: A new, long-wave formula for estimating downward clear-sky radiation at the surface. *Quart. J. Roy. Meteor. Soc.*, **122**, 1127–1151, doi:10.1002/qj.49712253306.

Rangwala, I., and J. R. Miller, 2012: Climate change in mountains: A review of elevation-dependent warming and its possible causes. *Climatic Change*, **114**, 527–547, doi:10.1007/s10584-012-0419-3.

Sakai, A., and Coauthors, 2006: Meteorological observation at July 1st glacier in northwest China from 2002 to 2005. *Bull. Glaciol. Res.*, **23**, 23–32.

Sedlar, J., and R. Hock, 2009: Testing longwave radiation parameterizations under clear and overcast skies at Storglaciären, Sweden. *Cryosphere*, **3**, 75–84, doi:10.5194/tc-3-75-2009.

Sicart, J. E., J. W. Pomeroy, R. L. H. Essery, and D. Bewley, 2006: Incoming longwave radiation to melting snow: Observations, sensitivity and estimation in northern environments. *Hydrol. Processes*, **20**, 3697–3708, doi:10.1002/hyp.6383.

——, R. Hock, P. Ribstein, and J. P. Chazarin, 2010: Sky longwave radiation on tropical Andean glaciers: Parameterization and sensitivity to atmospheric variables. *J. Glaciol.*, **56**, 854–860, doi:10.3189/002214310794457182.

Sun, W., X. Qin, Y. Xu, X. Wu, Y. Liu, and J. Ren, 2011: Annual variations of the components of radiation on the Laohugou No. 12 Glacier in the Qilian Mountains (in Chinese). *Adv. Earth Sci.*, **26**, 347–354. [Available online at http://www.adearth.ac.cn/EN/10.11867/j.issn.1001-8166.2011.03.0347.]

Swinbank, W. C., 1963: Long-wave radiation from clear skies. *Quart. J. Roy. Meteor. Soc.*, **89**, 339–348, doi:10.1002/qj.49708938105.

——, 1964: Long-wave radiation from clear skies. *Quart. J. Roy. Meteor. Soc.*, **90**, 488–493, doi:10.1002/qj.49709038617.

Tian, L., T. Yao, K. MacClune, J. W. C. White, A. Schilla, B. Vaughn, R. Vachon, and K. Ichiyanagi, 2007: Stable isotopic variations in west China: A consideration of moisture sources. *J. Geophys. Res.*, **112**, D10112, doi:10.1029/2006JD007718.

Unsworth, M. H., and J. L. Monteith, 1975: Long-wave radiation at the ground I. Angular distribution of incoming radiation. *Quart. J. Roy. Meteor. Soc.*, **101**, 13–24, doi:10.1002/qj.49710142703.

Van den Broeke, M., D. van As, C. Reijmer, and R. van de Wal, 2004: Assessing and improving the quality of unattended radiation observations in Antarctica. *J. Atmos. Oceanic Technol.*, **21**, 1417–1431, doi:10.1175/1520-0426(2004)021<1417:AAITQO>2.0.CO;2.

——, C. Reijmer, D. Van As, and W. Boot, 2006: Daily cycle of the surface energy balance in Antarctica and the influence of clouds. *Int. J. Climatol.*, **26**, 1587–1605, doi:10.1002/joc.1323.

Viúdez-Mora, A., J. Calbó, J. A. González, and M. A. Jiménez, 2009: Modeling atmospheric longwave radiation at the surface under cloudless skies. *J. Geophys. Res.*, **114**, D18107, doi:10.1029/2009JD011885.

——, M. Costa-Surós, J. Calbó, and J. A. González, 2015: Modeling atmospheric longwave radiation at the surface during overcast skies: The role of cloud base height. *J. Geophys. Res. Atmos.*, **120**, 199–214, doi:10.1002/2014JD022310.

Wacker, S., J. Gröbner, and L. Vuilleumier, 2014: A method to calculate cloud-free longwave irradiance at the surface based on radiative transfer modeling and temperature lapse rate estimates. *Theor. Appl. Climatol.*, **115**, 551–561, doi:10.1007/s00704-013-0901-5.

Wang, K., and S. Liang, 2009: Global atmospheric downward longwave radiation over land surface under all-sky conditions from 1973 to 2008. *J. Geophys. Res.*, **114**, D19101, doi:10.1029/2009JD011800.

Wang, W., and S. Liang, 2009: Estimation of high-spatial resolution clear-sky longwave downward and net radiation over land surfaces from MODIS data. *Remote Sens. Environ.*, **113**, 745–754, doi:10.1016/j.rse.2008.12.004.

Webster, C., N. Rutter, F. Zahner, and T. Jonas, 2016: Modeling subcanopy incoming longwave radiation to seasonal snow using air and tree trunk temperatures. *J. Geophys. Res. Atmos.*, **121**, 1220–1235, doi:10.1002/2015JD024099.

Yang, K., J. He, W. Tang, J. Qin, and C. C. K. Cheng, 2010: On downward shortwave and longwave radiations over high altitude regions: Observation and modeling in the Tibetan Plateau. *Agric. For. Meteor.*, **150**, 38–46, doi:10.1016/j.agrformet.2009.08.004.

Yang, W., X. Guo, T. Yao, K. Yang, L. Zhao, S. Li, and M. Zhu, 2011: Summertime surface energy budget and ablation modeling in the ablation zone of a maritime Tibetan glacier. *J. Geophys. Res.*, **116**, D14116, doi:10.1029/2010JD015183.

——, T. Yao, X. Guo, M. Zhu, S. Li, and D. B. Kattel, 2013: Mass balance of a maritime glacier on the southeast Tibetan Plateau and its climatic sensitivity. *J. Geophys. Res. Atmos.*, **118**, 9579–9594, doi:10.1002/jgrd.50760.

Yang, X., D. Qin, T. Zhang, S. Kang, X. Qin, and H. Liu, 2010: Seasonal characteristics of surface radiation fluxes on the East Rongbuk Glacier in the Mt. Everest region (in Chinese). *Acta Meteor. Sin.*, **24**, 680–698. [Available online at http://www.cmsjournal.net/qxxb_en/ch/reader/view_abstract.aspx?file_no=20100603&flag=1.]

Yao, T., and Coauthors, 2012: Different glacier status with atmospheric circulations in Tibetan Plateau and surroundings. *Nat. Climate Change*, **2**, 663–667, doi:10.1038/nclimate1580.

——, and Coauthors, 2013: A review of climatic controls on $\delta^{18}O$ in precipitation over the Tibetan Plateau: Observations and simulations. *Rev. Geophys.*, **51**, 525–548, doi:10.1002/rog.20023.

Zhang, G., and Coauthors, 2013: Energy and mass balance of Zhadang Glacier surface, central Tibetan Plateau. *J. Glaciol.*, **59**, 137–148, doi:10.3189/2013JoG12J152.

Zhu, M., T. Yao, W. Yang, F. Maussion, E. Huintjes, and S. Li, 2015: Energy- and mass-balance comparison between Zhadang and Parlung No. 4 Glaciers on the Tibetan Plateau. *J. Glaciol.*, **61**, 595–607, doi:10.3189/2015JoG14J206.